Materials Horizons

ROYAL SOCIETY OF CHEMISTRY

COMMUNICATION

View Article Online
View Journal | View Issue

Cite this: *Mater. Horiz.*, 2026, **13**, 3474

Received 10th October 2025,
Accepted 22nd January 2026

DOI: 10.1039/d5mh01916h

rsc.li/materials-horizons

Injectable hyaluronic acid-based hydrogels with carbon dots and an iron complex for embolization

Minyoung Jin, *[ab] Sanghee Lee,[cd] Yuhyeon Na,[ef] Hayoon Jeong,[g] Dong-Hyun Kim [dhij] and Kun Na *[ab]

Although transarterial chemoembolization is a prevalent treatment for hepatocellular carcinoma (HCC), its efficacy is limited by inadequate vascular infiltration, inconsistent embolization, and lack of therapeutic synergy. We developed a multifunctional injectable hydrogel system using strategically combined high- and low-molecular-weight hyaluronic acid and a carbon dot/iron complex (APIO/Fe complex) to overcome these challenges. The dual-molecular-weight approach optimizes both structural integrity and injectability and also enables the homogeneous distribution of therapeutic agents. The APIO carbon dots were produced by a one-pot hydrothermal synthesis using iohexol and 1-(3-aminopropyl) imidazole as dual-purpose precursors for computed tomography (CT) imaging and iron chelation. The APIO/Fe complex was characterized *via* dynamic light scattering, X-ray photoelectron spectroscopy, and transmission electron microscopy, confirming its nanoscale structure and compositional integrity. The APIO/Fe hydrogel demonstrated shear-thinning and self-healing properties, injectability, and mechanical recovery. The APIO/Fe complex and the hydrogel preserved CT and magnetic resonance imaging contrast capabilities compared with conventional contrast agents. They also catalyzed the Fenton reaction, initiated the formation of reactive oxygen species, and accelerated coagulation upon interaction with blood. In a three-dimensional vascular model, the APIO/Fe complex induced occlusion. This multifunctional platform integrates imaging visibility, oxidative therapy, and embolic function, thus providing a synergistic, minimally invasive approach for HCC treatment.

New concepts

In this study, a multifunctional injectable hydrogel based on hyaluronic acid, carbon dots and an iron complex was formulated as an embolic platform for integration of diagnosis and therapy. The injectable hydrogel introduces a novel approach to theragnostic embolization, enabling MRI/CT imaging and reactive oxygen species mediated tumor ablation. Unlike conventional embolic materials that serve as passive physical occlusions, this hydrogel actively participates in the therapeutic process through the iron mediated Fenton reaction, while maintaining excellent injectability and mechanical stability. While both hydrogels and metal based therapy have been individually explored for embolization, their integration into a single multifunctional platform has remained unexplored. This work demonstrates a synergistic design that leverages the contrast capability of carbon dots and the therapeutic reactivity of iron ions, thereby achieving both diagnostic visualization and antitumor efficacy within a single matrix.

1. Introduction

Hepatocellular carcinoma (HCC) is one of the most globally prevalent malignant tumors, associated with the sixth highest incidence rate and the third highest fatality rate among cancers.[1] Despite significant advances in early detection and treatment, HCC remains a substantial clinical challenge.[2,3] Although surgical resection represents the standard treatment choice, the majority of patients are ineligible due to the advanced tumor stage at diagnosis, underlying liver cirrhosis,

[a] *Department of BioMedical-Chemical Engineering, The Catholic University of Korea, Bucheon-si, Gyeonggi-do, 14662, Republic of Korea. E-mail: kna6997@catholic.ac.kr*
[b] *Department of Biotechnology, The Catholic University of Korea, Bucheon-si, Gyeonggi-do, 14662, Republic of Korea*
[c] *School of Nanomedical Engineering, Korea National University of Transportation, Chungju 27469, Republic of Korea*
[d] *Department of Radiology, Feinberg School of Medicine, Northwestern University, Chicago, IL, 60611, USA*
[e] *College of Pharmacy and Research Institute of Pharmaceutical Sciences, Seoul National University, Seoul 08826, Republic of Korea*
[f] *NBR incorporation, BI 205, Bucheon-si, Gyeonggi-do, 14662, Republic of Korea*
[g] *Dental Research Institute, School of Dentistry, Seoul National University, Seoul 03080, Republic of Korea*
[h] *Robert H. Lurie Comprehensive Cancer Center, Northwestern University, Chicago, IL, 60611, USA*
[i] *Department of Biomedical Engineering, McCormick School of Engineering, Northwestern University, Evanston, IL, 60208, USA*
[j] *Department of Biomedical Engineering, University of Illinois, Chicago, IL, 60607, USA*

or impaired hepatic function.[4,5] Consequently, supplementary and alternative treatments, including radiofrequency ablation (RFA) and transarterial chemoembolization (TACE), become essential for extending survival and improving the quality of life of the patient. RFA is effective for small, localized tumors, whereas TACE has established itself as the standard of care for patients with intermediate-stage HCC or those who are ineligible for surgery.[6–9] Nevertheless, when the tumor size increases or lesions are located near major vessels, the efficiency of RFA reduces dramatically.[10] In these cases, locoregional intra-arterial approaches using the liver's dual blood supply represent a more reliable technique for delivering treatment directly to the tumor site.

TACE operates by obstructing the hepatic artery that supplies the tumor, thereby triggering ischemia-induced cell death. Over time, standard embolization has evolved to encompass the intra-arterial administration of chemotherapeutic agents and supplementary irradiation.[11,12] These modalities aim at eliminating malignant cells by obstructing their vascular supply and administering cytotoxic agents directly into the tumor microenvironment. Nevertheless, current TACE techniques are restricted by the intrinsic properties of existing embolic materials, which often compromise the consistency and effectiveness of vascular occlusion.

Conventional embolic agents, including metallic coils, microspheres, and liquid embolics, exhibit specific limitations. Metallic coils, despite being accurately positioned, may inadequately obstruct convoluted vasculature, resulting in incomplete embolization or the development of collateral circulation.[13] Although microspheres can be infused with chemotherapeutic agents and provide more consistent size distribution, their rigidity may hinder appropriate conformation to intricate vessel geometries, and excessive distal embolization may cause damage to normal tissues.[14,15] Liquid embolics, such as cyanoacrylates and ethylene-vinyl alcohol copolymers, necessitate meticulous handling to prevent polymerization within the delivery catheter and may exert cytotoxic effects on adjacent tissues. Furthermore, the use of solvents such as dimethyl sulfoxide (DMSO) may exert adverse side effects.[16] These limitations emphasize the urgent need for innovative embolic systems that are biocompatible, nontoxic, adaptable to various vascular structures, and capable of providing prolonged occlusion, real-time imaging, and active tumoricidal functions.

Injectable hydrogels have emerged as promising candidates due to their advantageous characteristics for embolization.[17,18] Their soft, viscoelastic nature enables minimally invasive administration and adaptation to vascular architecture, thereby ensuring long-term retention. Moreover, injectable hydrogels can be designed to incorporate therapeutic agents, imaging contrast agents, or stimuli-responsive components, thus expanding their utility beyond mere mechanical blockage.[19] Multifunctional hydrogels have recently been developed for a wide range of biomedical applications, including sensing, regenerative engineering, and minimally invasive therapies.[20–22] However, several hydrogels experience rapid *in situ* gelation, resulting in uneven distribution or catheter blockage, particularly concerning the branched and narrow vasculature associated with HCC, where consistent occlusion is vital for therapeutic effectiveness.

Shear-thinning or self-healing injectable hydrogels present a feasible solution to these challenges. When shear stress is applied, these hydrogels display decreased viscosity, enabling smooth flow through narrow catheters. After the removal of stress, the hydrogels rapidly recover their original structure.[23,24] This rheological behavior ensures consistent distribution throughout the vascular network and reduces the risk of catheter blockage. Furthermore, shear-thinning hydrogels can be customized to incorporate capabilities such as drug delivery, multimodal imaging improvement, catalytic properties for localized tumor therapy, and procoagulant activity for improving the efficiency of embolization.[25,26]

Hyaluronic acid (HA) is a linear polysaccharide composed of repeating D-glucuronic acid and *N*-acetyl-D-glucosamine units, and plays essential physiological roles in tissue hydration, viscoelastic cushioning, lubrication, and extracellular-matrix organization.[27–29] Compared with other biopolymers, HA exhibits excellent biocompatibility and minimal immunogenicity,[30,31] and has been widely incorporated into FDA-approved injectable formulations. These favourable properties have led to the extensive use of HA-based materials in hydrogels, nanoparticles, wound healing, and cancer therapy platforms in recent research reports.[30,32–35]

The molecular weight of HA exerts a significant impact on the performance of hydrogels in embolization applications. High-molecular-weight HA provides superior viscoelastic properties, prolonged vascular retention through extensive intermolecular entanglements, and improved mechanical stability, rendering it ideal for structural support in embolic applications.[30,36] Nevertheless, high-molecular-weight HA often displays high viscosity that can impede injection through microcatheters and limit the distribution of therapeutic agents. Conversely, low-molecular-weight HA provides improved injectability, faster tissue penetration, and increased cellular interaction, thereby facilitating the delivery of drugs and the distribution of therapeutic agents. Therefore, the strategic integration of dual-molecular-weight HA could potentially optimize both mechanical performance and biological functionality, thus addressing the inherent trade-off between structural integrity and injectability that has restricted previous HA-based embolic systems.

To address these challenges, we describe a novel injectable hydrogel system composed of strategically combined high- and low-molecular-weight HA integrated with a carbon dot/iron (CD/Fe) complex. HA, a naturally occurring polysaccharide, is widely used in biomedical applications because of its superior biocompatibility, biodegradability, and ability to form hydrogels.[32,37,38] Moreover, the dual molecular weight of HA plays a vital role in determining the properties and injectability of the hydrogel. By integrating high and low-molecular-weight HA, the hydrogel provides not only structural integrity and prolonged retention but also improved injectability.

This HA-based hydrogel demonstrates shear-thinning characteristics and rapid structural recovery, allowing it to traverse

complex vascular networks without early solidification. In contrast to current embolic agents, the HA-APIO/Fe hydrogel is specifically engineered for improving endogenous thrombus formation through iron-mediated crosslinking of fibrinogen and platelet membranes, thereby providing physiologically reinforced closure for occluded arteries.

Carbon dots (CDs), a class of carbon-based nanomaterials generally measuring <10 nm in diameter, impart multifunctional properties to the hydrogel. They also exhibit excellent water solubility, low cytotoxicity, and tunable surface chemistry, rendering them highly attractive for biomedical applications, including imaging and drug delivery.[39,40] Moreover, surface functionalization with appropriate precursors improves their interaction with metal ions and other hydrogel components.[41,42] Upon complexation with iron ions, CDs facilitate the development of a stable nanocomposite network. Although iron coordination may quench the intrinsic fluorescence of CDs, this compromise is acceptable considering the aim of producing a multifunctional embolic system that integrates physical vascular occlusion with cytotoxic effects on cancer cells.

In this system, CDs serve a dual function. First, the iohexol-derived structure provides intrinsic computed tomography (CT) contrast.[40,43] Second, the abundant surface functional groups enable stable chelation with iron ions to form the APIO/Fe complex, thereby promoting reactive oxygen species (ROS) generation while preserving colloidal stability.[44,45]

The incorporated Fe ions perform multiple functions within the hydrogel matrix. Primarily, Fe ions improve imaging contrast, enabling precise embolic placement and real-time monitoring.[46,47] They also catalyze Fenton reactions, generating highly reactive hydroxyl radicals ($^{\bullet}OH$), a potent form of reactive oxygen species (ROS), that can trigger ferroptosis, an iron-dependent form of programmed cell death, along with other oxidative stress–related pathways.[48,49] This mechanism significantly increases cytotoxicity within the ischemic tumor microenvironment, thereby augmenting the therapeutic effects beyond those of conventional embolization. The HA-based hydrogel system described in this study, integrating both CDs and iron ions, accomplishes several essential functions, including (1) shear-thinning injectability for deep vascular penetration and uniform deposition, (2) formation of stable gel networks for durable vascular occlusion, (3) iron-mediated ROS generation to potentiate the destruction of tumor cells and improve the efficiency of treatment, (4) dual computed tomography (CT) and magnetic resonance imaging (MRI) contrast for real-time procedural guidance and postprocedural evaluation.

This study describes the successful integration of molecular-weight-optimized HA with iron-complexed CDs for advanced embolization therapy. The multifunctional hydrogel system, which combines the benefits of dual-molecular-weight HA, the multifunctionality of CDs, and the catalytic activity of iron ions, establishes a next-generation embolic material that provides both mechanical vascular occlusion and oxidative tumor destruction. This approach has considerable potential to overcome existing limitations in TACE and significantly improve clinical therapeutic outcomes for patients with HCC.

2. Results and discussion

Design of the APIO/Fe hydrogel

The APIO/Fe complex hydrogel was designed as a multifunctional embolic system through a systemic multistep synthesis strategy (Fig. 1a). The APIO (1-(3-aminopropyl)imidazole (API) and iohexol carbon dot) carbon dots (CDs) were synthesized through a one-pot hydrothermal reaction at 180 °C for 6 h as dual-purpose precursors. Iohexol was used as both the carbon source and the CT contrast,[40] and API was used to provide nitrogen-rich surface functionalities required for iron chelation and pH-responsive behavior.[50]

The subsequent complexation with iron ions resulted in stable APIO/Fe complexes, which were then incorporated into a strategically designed dual-molecular-weight HA matrix. The final hydrogel system combined high-molecular-weight HA (260 kDa) for structural integrity and prolonged retention with low-molecular-weight HA (0.5–10 kDa) for improved injectability and cellular interaction, thereby achieving an optimal balance between mechanical stability and processability.

The integrated capabilities of the APIO/Fe complex hydrogel for HCC treatment are depicted in Fig. 1b. The APIO/Fe complex hydrogel enables catheter-based delivery thorough hepatic arteries, provides immediate physical vascular occlusion, and simultaneously generates ROS through iron-catalyzed Fenton reactions. The incorporated functionalities of CDs and the iron complex provide dual-modal CT and MRI contrast abilities and enable real-time monitoring and post-treatment evaluation of the distribution and retention of embolic agents.

Physicochemical characterization of APIO and APIO/Fe complex

We performed a comprehensive physiochemical characterization to confirm successful APIO synthesis and APIO/Fe complex formation. Dynamic light scattering (DLS) (Fig. 2a) revealed that pristine APIO exhibited an average hydrodynamic diameter of approximately 1 nm, which is an ultrasmall and highly dispersed nanoparticle. Upon complexation with iron ions, the size distribution shifted significantly to an average diameter of approximately 8 nm, confirming successful complex formation along with maintaining a suitable nanoscale size for vascular applications and cellular interaction. Transmission electron microscopy (TEM) images of APIO (Fig. 2b) and APIO/Fe complex (Fig. 2e) revealed the nanostructures of APIO and APIO/Fe complex, thereby corroborating the results of DLS. Zeta potential analysis (Fig. 2d) provided evidence of complex formation between APIO and iron ions. APIO exhibited a negative surface charge of -7.7 mV, which is attributed to deprotonated carboxyl and hydroxyl groups on the surface. Upon iron complexation, there was a dramatic inversion in charge to $+48.3 \pm 3.2$ mV. The surface charge reversal from negative to positive after complexation is attributed to the strong coordination of iron ions with anionic surface groups of APIO. This coordination neutralizes the original negative charges and results in charge overcompensation, producing a positive ζ-potential. To further verify the elemental composition of

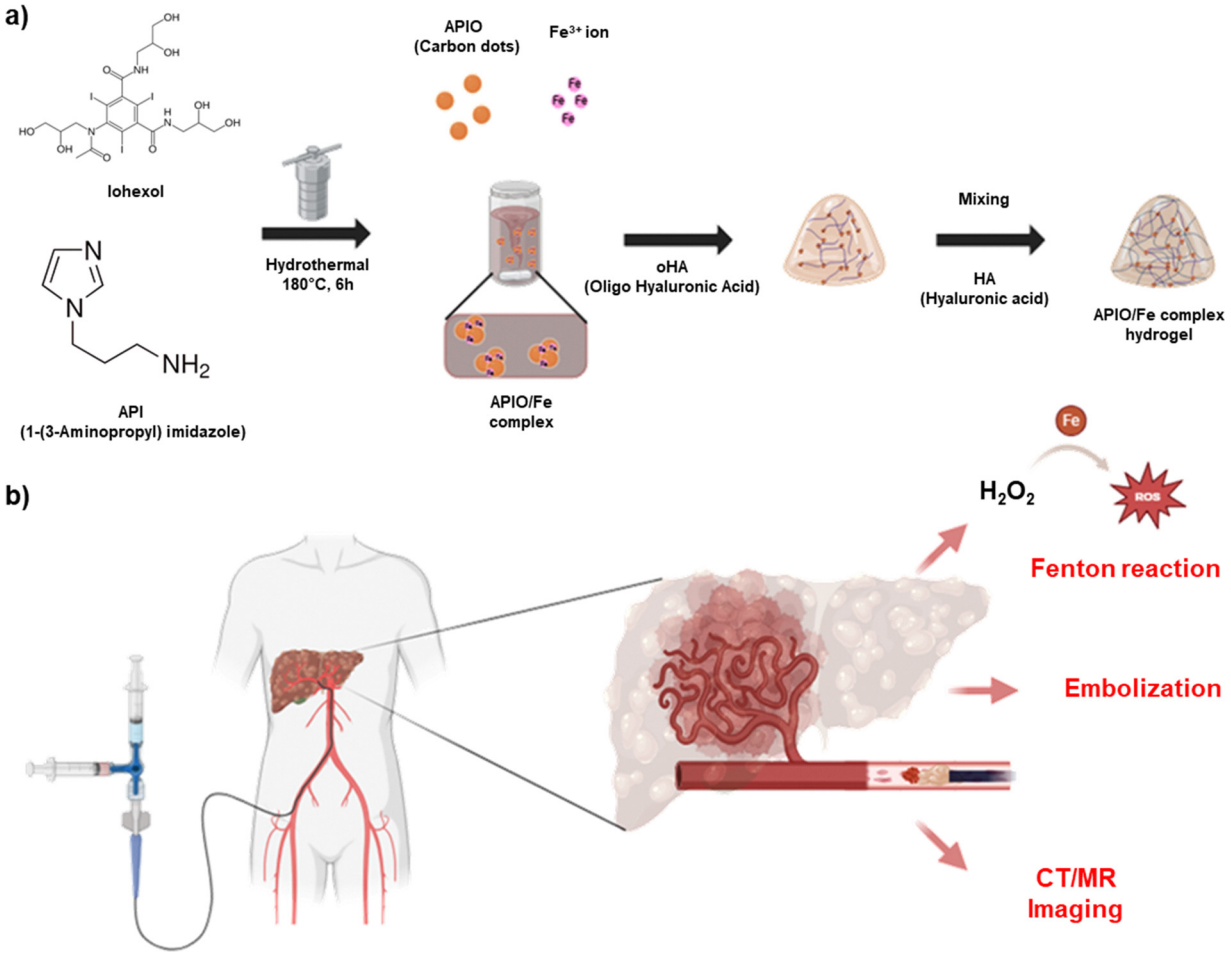

Fig. 1 Synthesis and application of the APIO ((1-(3-aminopropyl) imidazole (API) and iohexol carbon dot))/Fe complex hydrogel for embolization. (a) Synthesis procedure of the APIO/Fe complex hydrogel. (b) Application of the APIO/Fe complex hydrogel in embolization. Graphical images were generated using BioRender.com.

the APIO and APIO/Fe complex, inductively coupled plasma mass spectrometry (ICP-MS) was performed. APIO contained 13.45% iodine whereas the APIO/Fe complex contained 8.24% iron. These quantitative results support both the CT contrast capability of APIO and the successful iron complexation in the APIO/Fe complex, consistent with the observed changes in particle size and surface charge. The enlargement of particle size from APIO to the APIO/Fe complex can be attributed to the multidentate coordination behavior of iron ions. Since each iron ion can simultaneously bind multiple surface functional groups, several APIOs become interconnected through Fe-mediated bridging, forming a compact nanocluster structure.[44,51,52] This coordination driven complex is consistent with the observed changes in particle size and surface charge.

Surface chemistry coordination analysis

Iron incorporation and surface chemical modification were confirmed by X-ray photoelectron spectroscopy (XPS) (Fig. 2c and f). The APIO survey spectrum exhibited characteristic peaks for carbon (C 1s, 285 eV), oxygen (O 1s, 532 eV), nitrogen (N 1s, 400 eV), and iodine (I $3d_{5/2}$ and I $3d_{3/2}$, 630 and 619 eV), confirming the successful incorporation of both precursor molecules and retention of iohexol-derived functionalities vital for CT imaging contrast.[40,53,54] The APIO/Fe complex spectrum demonstrated not only all the characteristic peaks of APIO but also iron-specific peaks with Fe $2p_{3/2}$ and Fe $2p_{1/2}$ appearing at 711 and 724 eV, respectively. The binding energy positions and peak shapes were consistent with iron ions in a coordination environment, supporting chelation mechanisms rather than simple physical adsorption. The Fe $2p_{3/2}$ and $2p_{1/2}$ peaks, which were absent from the APIO spectrum, further confirmed successful iron incorporation. The binding energy positions of these peaks were consistent with those of chelated iron ions.[55,56] Atomic percentage analysis revealed approximately 3.2% iron content, indicating successful but controlled iron incorporation that maintains the structure of CDs and also provides sufficient catalytic activity for therapeutic applications.

To gain deeper insights into the surface chemistry and coordination environment, we obtained high-resolution XPS spectra for all major elements of APIO and APIO/Fe complex (Fig. S1). The deconvoluted C 1s spectrum (Fig. S1a) and the O 1s spectrum of APIO (Fig. S1b) showed that the CD contains

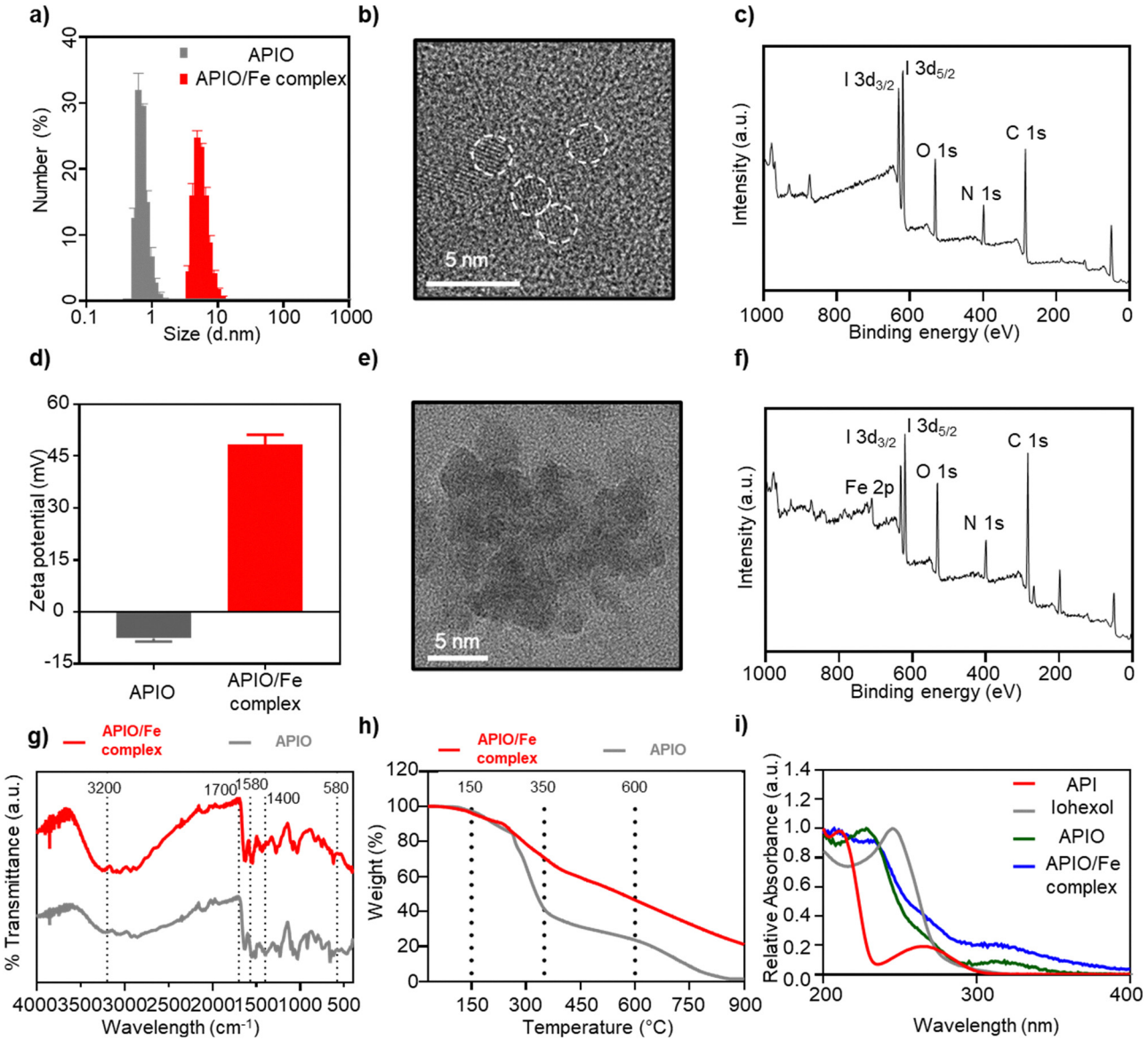

Fig. 2 Characterization of APIO and APIO/Fe complex. (a) Size distribution obtained by dynamic light scattering. (b) Transmission electron microscopy (TEM) image of APIO. (c) Full X-ray photoelectron spectroscopy (XPS) spectrum of APIO. (d) Zeta potential of APIO and APIO/Fe complex. (e) TEM image of APIO/Fe complex. (f) Full XPS spectrum of APIO/Fe complex. (g) FTIR spectrum of APIO and APIO/Fe complex. (h) TGA of APIO and APIO/Fe complex. (i) UV-vis spectrum analysis.

various carbon- and oxygen-containing functional groups such as carboxyl and hydroxyl groups for iron coordination. The N 1s spectrum (Fig. S1c) exhibited peaks corresponding to pyridinic nitrogen (398.7 eV) and pyrrolic nitrogen (400.2 eV), indicating the successful incorporation of nitrogen functionalities that contribute to iron chelation.[57,58] The I 3d spectrum of APIO (Fig. S1d) confirmed the presence of iodine with characteristic I $3d_{5/2}$ and I $3d_{3/2}$ peaks at 619.1 and 630.6 eV, respectively, thus validating the preservation of CT contrast functionality in the final structure of the CD.

For the APIO/Fe complex, the high-resolution spectra revealed significant changes in surface chemistry (Fig. S1e–i). The C 1s spectrum (Fig. S1e) revealed shifts in binding energies and relative intensities, particularly for C–O and C═O components, indicating their involvement in iron coordination. The O 1s spectrum (Fig. S1f) exhibited a single, broader peak at 531.8 eV, suggesting the coordination of oxygen atoms to iron centers.

Most critically, the Fe 2p spectrum (Fig. S1i) provided detailed information regarding iron oxidation states and coordination environments. Deconvolution revealed multiple iron species with Fe $2p_{3/2}$ peaks at ~710.8 and ~712.4 eV, corresponding to different Fe^{3+} coordination environments, and Fe $2p_{1/2}$ peaks at ~724.2 and ~725.8 eV. The absence of significant Fe^{2+} contributions (which would appear at ~709 eV for Fe $2p_{3/2}$) confirmed that iron exists predominantly in the Fe^{3+} oxidation state, optimal for Fenton catalysis.

Quantitative analysis of the Fe 2p spectrum revealed the distribution of iron oxidation state (Fig. S2). Peak deconvolution

and area integration showed that Fe^{3+} species constituted 70.91% of total iron content, whereas Fe^{2+} constituted 30.36%. This Fe^{3+}-dominant composition is ideal for catalytic applications, because Fe^{3+} serves as the active species in Fenton reactions, and the minor Fe^{2+} component can participate in Fenton-like reactions and contribute to the overall catalytic efficiency.

The binding energy values and peak shapes indicate that iron exists in a coordinated environment rather than as separate oxide phases, thereby supporting the proposed chelation mechanism. The predominance of Fe^{3+} also explains the positive zeta potential observed for the APIO/Fe complex, because coordinated Fe^{3+} centers contribute significant positive charge to the particle surface.

Fourier transform infrared (FTIR) spectroscopy and coordination mechanism

FTIR spectroscopy revealed detailed insights into the coordination chemistry and bonding mechanisms (Fig. 2g). The APIO spectrum exhibited characteristic features, including broad O–H stretching vibrations (3200–3500 cm^{-1}),[59–62] C=O stretching from carboxyl/amide groups (1700 cm^{-1}),[59,63] and C–O stretching from alcohol/epoxy functionalities (1000–1300 cm^{-1}).[63,64] After iron complexation, several key spectral changes were observed, such as (1) weakening and narrowing of the O–H band, indicating the involvement of hydroxyl groups in coordination, (2) conversion of the single C=O band into asymmetric ($\sim$1580 cm^{-1}) and symmetric ($\sim$1400 cm^{-1}) COO^- stretching modes, characteristic of carboxylate–metal coordination, and (3) emergence of a new band at $\sim$580 cm^{-1}, attributable to Fe–O or Fe–O–C coordination bonds.[65,66] This coordination mode is consistent with the findings of XPS that showed Fe^{3+} in multiple coordination environments, probably reflecting different binding sites on the surface of CDs and allowing controlled iron release for catalytic activity.

Thermogravimetric analysis for structural characterization and complex formation verification

Thermogravimetric analysis (TGA) was conducted to confirm the formation of the APIO/Fe complex and clarify the structural changes upon iron coordination (Fig. 2h). The TGA profiles revealed distinct decomposition patterns that confirmed successful complex formation. APIO CDs displayed a characteristic decomposition profile at 150 °C, which is attributed to the removal of water and volatile organic components.[67] The major decomposition occurred between 150 °C and 350 °C with approximately 56% mass loss in the APIO group, corresponding to the thermal degradation of surface functional groups, including carboxyl, hydroxyl, and amine functionalities.[68] The final residue at 900 °C was minimal at approximately 1.7%, consistent with the predominantly organic nature of CDs and confirming their complete combustion.

In contrast, the APIO/Fe complex presented a markedly different decomposition profile that provides evidence for iron incorporation and coordination bonding. The onset of decomposition shifted, indicating that iron coordination stabilizes the surface functional groups against thermal degradation. The mass loss pattern showed that iron coordination prevented the facile decomposition of surface functionalities. The most compelling evidence for complex formation originated from the final residue analysis. APIO left only 1.7% residue, whereas the APIO/Fe complex yielded 21.1% residue at 900 °C. This substantial increase in residue content directly corresponds to the formation of thermally stable iron oxide species upon high-temperature decomposition of the organic components. The results of TGA provided critical evidence that the APIO/Fe system represents a genuine coordination complex rather than a physical mixture of components.

Optical properties and electronic structure modifications

UV-visible absorption spectroscopy demonstrated the optical characteristics and confirmed the successful synthesis of both precursor materials and the final complex (Fig. 2i). Individual precursors (API and iohexol) exhibited distinct absorption profiles, with API showing characteristic absorption at approximately 280 nm and iohexol displaying broad absorption in the UV region. APIO CDs demonstrated typical CD absorption features comprising two primary bands, at approximately 230 and 320 nm, respectively. The APIO/Fe complex exhibited modified optical properties with improved absorption intensity across the UV-visible spectrum and slight redshifting of absorption, which revealed the formation of the CD/metal complex.[69]

Comprehensive characterization data, including high-resolution XPS analysis and quantification of the iron oxidation state, collectively confirmed the successful formation of the APIO/Fe complex through surface-level electrostatic and coordination interactions. The predominance of iron ions in the APIO/Fe complex confirmed its formation for Fenton catalysis–based therapeutic applications. The detailed surface chemistry analysis provided critical insights into the coordination mechanism and validated the design strategy for producing stable, catalytically active CD–Fe complexes suitable for biomedical applications.

ROS generation and therapeutic mechanism validation

The therapeutic potential of the APIO/Fe complex was determined through comprehensive mechanistic studies and cytotoxicity assays (Fig. 3). Direct evidence for the formation of $^{\bullet}OH$ radicals was obtained through electron paramagnetic resonance (EPR) spectroscopy using 5,5-dimethyl-1-pyrroline N-oxide (DMPO) as a spin trap agent (Fig. 3a). The APIO/Fe complex in the presence of H_2O_2 exhibited the characteristic 1 : 2 : 2 : 1 quartet signal pattern with hyperfine coupling constants typical of DMPO–OH adducts.[70,71] Control experiments revealed minimal or no EPR signals for H_2O_2 alone, APIO alone, or the complex without H_2O_2, thereby confirming that $^{\bullet}OH$ generation requires both the iron catalyst and hydrogen peroxide substrate. This definitive spectroscopic evidence validated the proposed Fenton reaction mechanism and established the APIO/Fe complex as an effective catalyst for the therapeutic generation of ROS.

To verify whether the APIO/Fe complex retains catalytic and biological activity within the hydrogel matrix, additional experiments were performed using extracts prepared from the

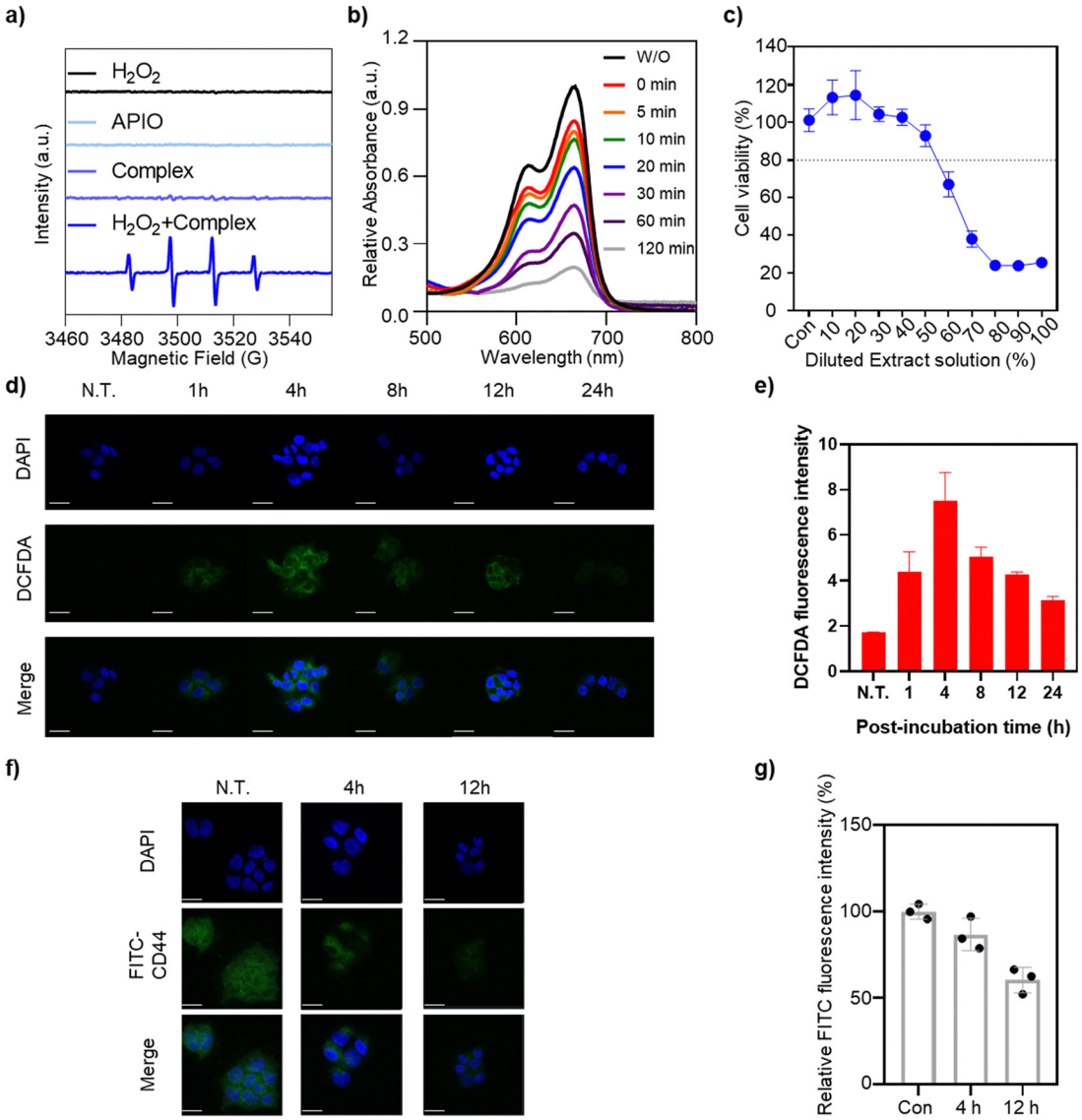

Fig. 3 Fenton reaction of the APIO/Fe complex and APIO/Fe complex hydrogel extract. (a) DMPO spin trapping EPR spectra of •OH radicals in the Fenton reaction. (b) Fenton reaction assay *via* methylene blue degradation using APIO/Fe hydrogel extracts. (c) Cell viability assay of APIO/Fe hydrogel extracts. (d) Representative fluorescence images of ROS detection by fluorescence intensity of DCFDA stained HepG2 cells (n = 3, scale bar: 50 μm). (e) Fluorescence intensity of DCFDA from the result d. (f) Representative fluorescence images of lipid peroxidation by fluorescence intensity measurement. (g) Relative FITC fluorescence intensity from the result f (n = 3, scale bar: 50 μm).

APIO/Fe hydrogel. The iron release profile demonstrated that approximately 8.88% of the total iron content was released within 24 h (Fig. S3). The resulting extract was subsequently diluted to an iron concentration of 1 mM, identical to the concentration applied in APIO/Fe nanocomplex-only experiments, allowing direct comparison of cytotoxicity and ROS-generating performance.

The catalytic activity of the APIO/Fe hydrogel for the Fenton reaction was evaluated using hydrogel extracts through a methylene blue degradation assay, which serves as a reliable indicator of •OH generation.[72] As depicted in Fig. 3b, the extract exhibited time-dependent reduction of methylene blue in the presence of H_2O_2, demonstrating that the iron species released from the hydrogel retain Fenton activity.

To confirm that this activity originates from the APIO/Fe complex, methylene blue degradation was subsequently measured using the APIO/Fe complex at the same iron concentration (Fig. S4). As expected, the APIO/Fe complex induced a rapid decrease in methylene blue absorbance, reflecting the immediate accessibility of catalytic sites once directly exposed to H_2O_2. In contrast, the hydrogel extract displayed more gradual degradation due to the presence of free HA and other extractable hydrogel components, which can hinder the diffusion of hydroxyl radicals. Despite these differences, both the APIO/Fe complex and hydrogel extract effectively degraded methylene blue, confirming that iron released from the hydrogel maintains full catalytic competence for ROS generation.

Cytotoxicity evaluation

The therapeutic efficacy of the APIO/Fe complex and the APIO/Fe complex hydrogel was evaluated using HepG2 HCC cells (Fig. 3c and Fig. S5). As shown in Fig. 3c, the hydrogel extract exhibited dose-dependent reduction in cell viability at extract concentration above 60%. To determine whether this behavior was consistent with the APIO/Fe complex, additional experiments were performed using the APIO/Fe complex (Fig. S5). The APIO/Fe complex exhibited a steep decrease in cell viability from 6 mM of iron concentration, suggesting potent anticancer activity. Notably, cytotoxicity appeared at 60% extract, which corresponds to an iron level similar to the concentration at which the APIO/Fe complex also exhibited cytotoxicity. These results demonstrate that hydrogel released species such as the APIO/Fe complex maintain comparable therapeutic activity.

Intracellular ROS accumulation and temporal dynamics

To visualize and quantify the intracellular generation of ROS, HepG2 cells were treated with APIO/Fe hydrogel extracts and APIO/Fe complex and examined using 2′,7′-dichlorofluorescin diacetate (DCFDA) staining (Fig. 3d, e and Fig. S6). For direct comparison, the hydrogel extracts were diluted to match the iron concentration used in the APIO/Fe complex treatment. Time-course fluorescence microscopy revealed progressive accumulation of intracellular ROS over 24 h. Untreated control cells (N.T.) displayed minimal green fluorescence, indicating baseline ROS levels. Quantitative analysis of DCFDA fluorescence intensity (Fig. 3e) confirmed strong green fluorescence that appeared as early as 1 h post-incubation followed by a gradual decline after 8 h (Fig. S6), confirming that the observed ROS originates from the catalytic activity of the APO/Fe complex. This temporal profile demonstrated sustained ROS generation that is sufficient for therapeutic intervention while providing insights into the kinetics of oxidative stress induction.

CD44 expression and membrane integrity evaluation

ROS-induced membrane damage was assessed using FITC-conjugated anti-CD44 antibody (Fig. 3f, g and Fig. S7). CD44, a major HA receptor expressed on HepG2 cell membranes serves as an indicator of membrane stability and cellular viability.[73,74] Control cells (N.T.) exhibited strong, uniform green fluorescence, indicating high CD44 expression levels on intact cell membranes. In contrast, treatment with the hydrogel extract and APIO/Fe complex exhibited progressive reduction in CD44 fluorescence intensity over time. Quantitative analysis revealed 13% reduction at 4 h and 39% reduction at 12h, demonstrating gradual ROS-mediated membrane destabilization (Fig. 3f and g). The hydrogel extract concentration was adjusted to provide an iron level equivalent to that of the APIO/Fe complex, and a similar decrease was observed when cells were treated with the APIO/Fe complex at the same iron concentration (Fig. S7).

This progressive loss of CD44 expression indicates ROS-mediated membrane damage. Lipid peroxidation causes membrane destabilization and protein dissociation, while direct oxidative modification of CD44 disrupts antibody recognition.[75–77] The temporal correlation between ROS accumulation (Fig. 3d and e) and CD44 loss (Fig. 3f and g) demonstrated that oxidative membrane damage is a primary mechanism of the APIO/Fe complex induced cytotoxicity. Importantly, the parallel results in intracellular ROS accumulation and ROS-induced membrane damage confirm that the released APIO/Fe complexes retain their catalytic functionality, demonstrating functional equivalence between the released fraction from the hydrogels and the APIO/Fe complex.

Rheological properties and mechanical characterization

We comprehensively evaluated the rheological properties of the APIO/Fe complex hydrogel to determine its suitability as an injectable embolic agent for TACE procedures (Fig. 4). These mechanical characteristics are crucial for ensuring both successful catheter delivery and effective vascular occlusion upon deployment. Frequency sweep analysis revealed that the APIO/Fe complex hydrogel displayed a predominantly elastic behavior across physiologically relevant conditions (Fig. 4a). At both room temperature (RT, 25 °C) and physiological temperature (37 °C), the storage modulus (G') consistently exceeded the loss modulus (G'') across the entire tested frequency range. This elastic dominance ($G' > G''$) confirmed the formation of a stable three-dimensional network structure for effective vascular occlusion.[78,79] Remarkably, the moduli values increased at physiological temperature, indicating improved network stability under *in vivo* conditions, which is beneficial for maintaining embolic integrity after deployment.[80]

Gelation kinetics and network formation

The time-dependent gelation behavior was evaluated to determine the rapid network formation capability of the APIO/Fe complex hydrogel (Fig. 4b). The gelation profile demonstrated that G' exceeded G'' within approximately 4 min at 37 °C, indicating rapid formation of the gel network that is suitable for immediate vascular occlusion upon injection. After the crossover point ($G' = G''$) occurred, both moduli continued to increase within 15 min. This rapid gelation kinetic ensures that the hydrogel can quickly transition from an injectable liquid-like state to a solid-like embolic mass, preventing premature washout and also allowing sufficient time for catheter positioning and injection.

Viscosity optimization and temperature dependence

The contribution of individual components to the overall rheological behavior was determined by comparative viscosity analysis (Fig. 4c). Native HA demonstrated relatively low viscosity (268.8 mPa s at 1 Hz), whereas incorporation of the APIO/Fe complex significantly increased the viscosity to 347.7 mPa s. This increase reflects the formation of additional crosslinks through iron-mediated coordination with HA chains and APIO CDs, thus producing a more robust network structure.

The temperature-dependent viscosity of APIO/Fe complex hydrogel measurements (Fig. 4d) revealed a beneficial

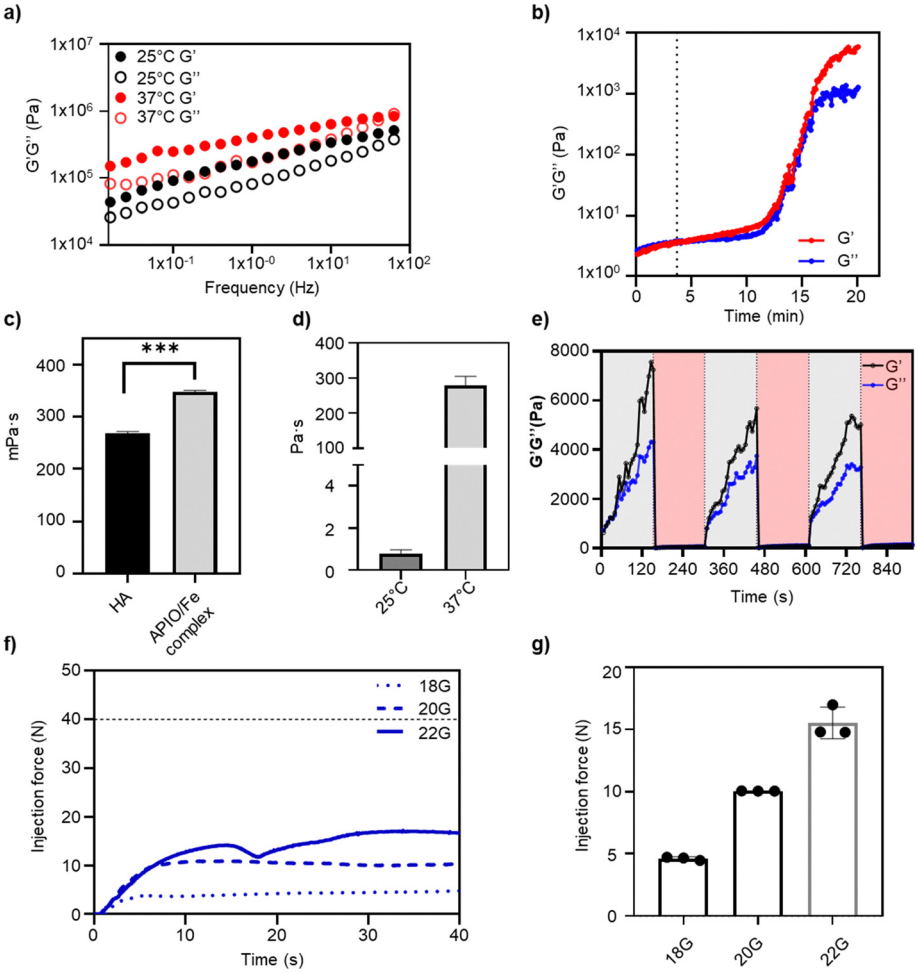

Fig. 4 Rheological properties of APIO/Fe complex hydrogel. (a) Storage (G') and loss (G'') modulus of APIO/Fe complex gel at 25 °C and 37 °C (Strain: 0.1%, Frequency: 0.01–100 Hz). (b) Gelation time of APIO/Fe complex hydrogel (1% strain, 1 Hz). (c) Viscosity value of HA and APIO/Fe complex hydrogel (1 Hz). (d) Relative complex viscosity value of APIO/Fe complex gel at 25 °C and 37 °C (strain: 0.1%, Frequency: 1 Hz). (e) Recovery test of the APIO/Fe complex hydrogel. (f) Injection force graph of APIO/Fe complex hydrogel with different sizes of needles (Flow: 1 mL min^{-1}, Room temperature). (g) Injection force results of APIO/Fe complex gel with different sizes of injection needles (n = 3, Flow: 1 mL min^{-1}, measured at 30 s, room temperature).

thermosensitive response. When the temperature increased from 25 °C to 37 °C, the viscosity of the complex increased from 0.8 to 279.3 Pa s, indicating a dramatic increase. The temperature dependent shift reflects accelerated network relaxation arising from enhanced polymer chain mobility, weakened intermolecular hydrogen bonding, and the increased exchange kinetics of the dynamic Fe-ligand coordination bonds, consistent with previously reported thermally activated coordination driven hydrogel systems.[81–83] In addition, this temperature-responsive behavior is advantageous for embolization applications, because it ensures low viscosity during handling and injection at RT, followed by a rapid increase in viscosity upon reaching body temperature, thereby improving intravascular retention and reducing the risk of distal migration.

Self-healing and recovery properties

The self-healing capability of the APIO/Fe complex hydrogel was determined using cyclic strain recovery tests (Fig. 4e). The hydrogel was exposed to alternating low-strain (0.1%, pink regions) and high-strain (100%, gray regions) conditions to simulate the mechanical stresses encountered during injection and deployment. After each high-strain cycle, G' and G'' rapidly recovered to their initial values within seconds, demonstrating excellent self-healing properties. This remarkable recovery behavior indicated that the hydrogel network can withstand the shear forces encountered during catheter injection and also rapidly reestablish its structural integrity.[84–86] The complete recovery of mechanical properties after multiple cycles confirmed the reversible nature of the crosslinks, probably involving both physical entanglements and dynamic coordination bonds between iron and HA/APIO components. This self-healing capability is vital for maintaining embolic effectiveness even after experiencing high shear stress during delivery. The shear-thinning behavior and self-recovery properties in the APIO/Fe complex hydrogel arise from the synergistic interplay between dual-molecular-weight HA and dynamic metal–ligand coordination. The high molecular weight HA provides an

extensive chain entangled backbone, while the low molecular weight HA reduces viscosity and facilitates iron diffusion within the polymer matrix.[87–89] In addition, the iron ions coordinate simultaneously with carboxylate groups on the HA chains and functional groups on APIO carbon dot surfaces which create a reversible metal–ligand coordination network.[90–92] Under shear stress, these coordination bonds transiently dissociate, allowing HA and APIO to slip relative to each other, thereby enabling smooth flow through narrow catheters. Once the stress is removed, the iron ions rapidly reassociate with HA and APIO, leading to recovery of the network structure. This dynamic coordination mechanism, distinct from simple physical polymer mixing, fundamentally enables the balancing of injectability with mechanical stability essential for effective vascular embolization.

Additionally, the long-term viscosity stability of the APIO/Fe hydrogel was evaluated under physiological mimicking conditions (Fig. S8). The hydrogel retained approximately 53.9% of its initial complex viscosity after 15 days (from 56.1 to 30.2 mPa s). Notably, this viscosity value remains comparable to several clinically used liquid embolic systems including Lipiodol (20 to 40 mPa s), which typically lose flow resistance within hours to several days.[93–95] These results indicate that the APIO/Fe hydrogel maintains physiologically relevant viscosity for a substantially longer period, supporting its potential for durable vascular occlusion in embolization applications.

Injectable delivery and needle compatibility

We next examined the clinical applicability of the APIO/Fe complex hydrogel through comprehensive injectability studies using needles of varying gauge sizes (Fig. 4f, g and Fig. S9). Monitoring of the injection force at a rate of 1 mL min^{-1} revealed gauge-dependent force requirements. Quantitative analysis of injection forces (measured at 30 s) showed that the injection force did not exceed 20 N in all needle gauges. The APIO/Fe complex hydrogel displayed easy injectability, requiring much less force than the maximum physical threshold for injectable biomaterials. Although 64 N is considered the upper physical limit for injection using clinical needles, our hydrogel can be delivered using much lower effort within the recommended clinical range for smooth and safe interventional procedures (<20 N).[96–98]

Visual assessment of injectability (Fig. S9) confirmed successful delivery through all tested needle gauges. Importantly, the APIO/Fe complex hydrogel did not cause any needle clogging, fragmentation, or phase separation, indicating excellent processability and clinical compatibility.

Bimodal contrast properties

To investigate the potential of the APIO/Fe complex as a dual-modal contrast agent for image-guided therapy, we systematically

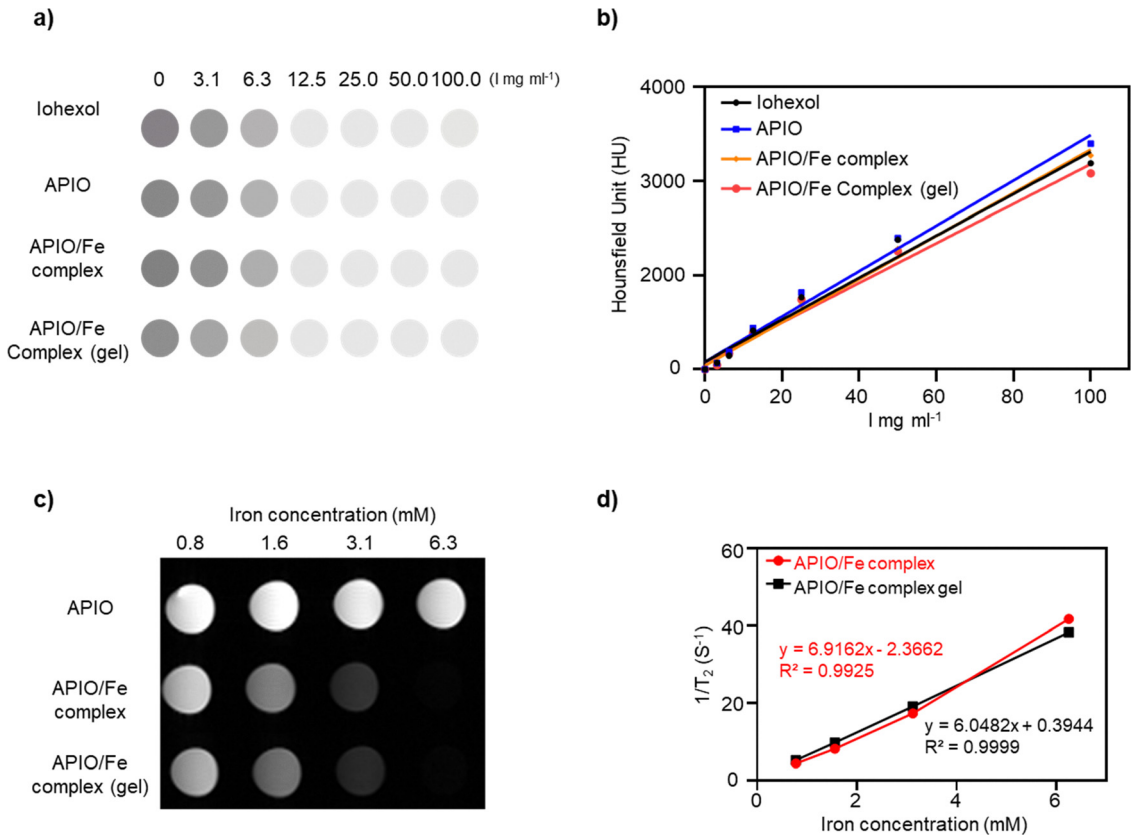

Fig. 5 Imaging capabilities of APIO/Fe complex gel. (a) *in vitro* CT imaging of iohexol, APIO, APIO/Fe complex and APIO/Fe complex gel. (b) X-ray attenuation linear coefficient with iodine concentration. (c) T_2-weighted MR images of APIO, APIO/Fe complex and APIO/Fe complex gel. (d) Plot of R^2 value of APIO/Fe complex and APIO/Fe complex gel.

evaluated both CT and MRI capabilities. For CT imaging evaluation, we serially diluted iohexol, APIO, APIO/Fe complex and APIO/Fe complex hydrogel to establish concentration-dependent contrast profiles (Fig. 5a and b). The Hounsfield unit (HU) values increased linearly with iodine concentration for all materials, confirming preserved X-ray attenuation properties after carbonization and iron complexation. Remarkably, the APIO/Fe complex hydrogel exhibited similar CT contrast efficiency compared to other samples including iohexol. These results demonstrate that the APIO/Fe complex hydrogel is suitable for real-time procedural guidance.

For MRI performance evaluation, the APIO/Fe complex solutions and hydrogels were evaluated using a 9.4-T animal MRI system with various iron concentrations (Fig. 5c and Fig. S10). T_2-weighted images revealed progressive signal darkening with increasing iron concentrations, characteristic of superparamagnetic contrast agents. Conversely, T_1-weighted images revealed mild brightening effects, indicating dual T_1/T_2 contrast capability. Quantitative relaxivity analysis (Fig. 5d) yielded r_2 values of 6.92 mM^{-1} s^{-1} for the APIO/Fe complex and 6.05 mM^{-1} s^{-1} for the hydrogel formulation, both of which exceeded the clinical standard Omniscan (4.93 mM^{-1} s^{-1}, Fig. S11). These results established the APIO/Fe complex hydrogel as an effective dual-modal (CT/MRI) contrast platform, which enables simultaneous visualization during embolization procedures and post-treatment monitoring, a critical advancement over current single-modality embolic agents.[99–101]

Enhanced coagulation and thrombogenicity

Quantitative coagulation assays were performed to determine whether the APIO/Fe complex hydrogel accelerates thrombus formation and improves embolic stability (Fig. 6a). According to established protocols,[102–106] fresh mouse whole blood was collected in tubes containing sodium citrate as an anticoagulant. Prepared samples were then placed into tubes and incubated for 5 min. Next, 1 mL of deionized (DI) water was gently added to each tube to lyse any erythrocytes not entrapped within the clot. After inverting and centrifugation, the absorbance of each supernatant was measured. The blood clotting index (BCI) was calculated using the following equation: BCI = [absorbance_sample/absorbance_control] × 100%).

The APIO/Fe complex hydrogel exhibited remarkable procoagulant activity, reducing the BCI to <10% compared with saline control (100%), indicating >90% clot formation efficiency (Fig. 6b and c). This improved thrombogenicity arises from two synergistic mechanisms. One is the electrostatic capture of fibrinogen and platelets through the positively charged APIO/Fe complex surface, facilitating rapid protein adsorption and platelet activation, and the other mechanism is the catalytic crosslinking mediated by trivalent iron ions, which promote intermolecular fibrin mesh tightening and

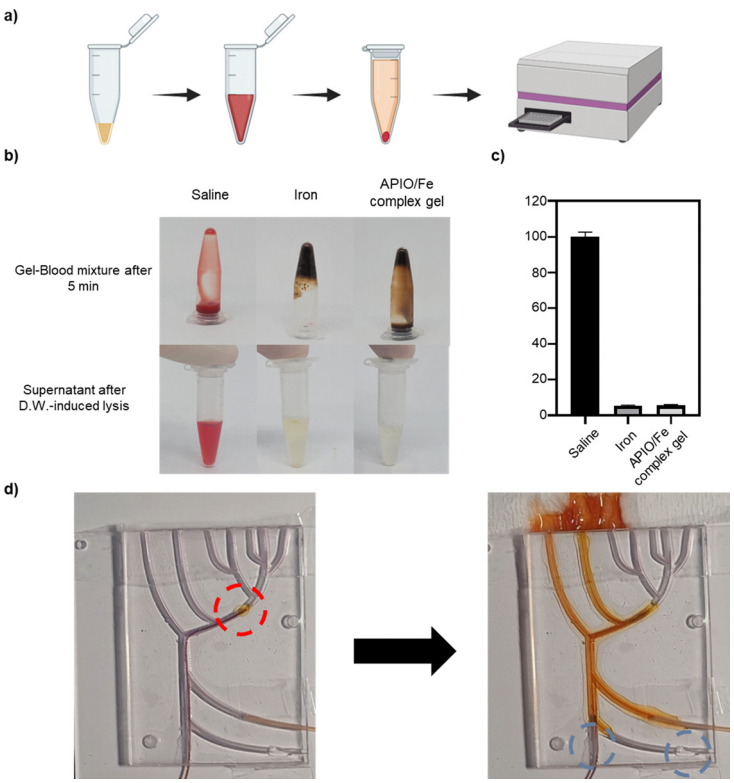

Fig. 6 Embolization efficacy of the APIO/Fe complex hydrogel. (a) Schematic illustration of coagulation assay. (b) Photographs of blood coagulation treated with the prepared hydrogels after 5 min. (c) Blood clotting index (BCI) of the samples at 540 nm absorbance (n = 4), BCI (%) = [absorbance_sample/absorbance]_ control] × 100. (d) Embolization effect of APIO/Fe complex gel in 3D vascular model. Red circle: APIO/Fe complex gel. Blue circle: sealing site with gelatin.

increased erythrocyte trapping through coordination chemistry. This dramatic increase in coagulation places the APIO/Fe hydrogel as a biologically active embolic agent that forms durable, mechanically reinforced clots, thus potentially reducing postprocedural recanalization rates.

3D vascular model of embolization efficacy

To simulate clinical embolization conditions, we designed a polydimethylsiloxane (PDMS) 3D vascular model replicating the branched arterial architecture encountered in hepatic TACE procedures. The APIO/Fe complex hydrogel was injected using a 2.8-Fr microcatheter while blood-mimicking fluid (BMF) flowed at physiological rates (1 mL min^{-1}) to determine occlusion efficacy under dynamic conditions (Fig. 6d and Fig. S12). The BMF solution was prepared based on previously reported papers.[107] In the absence of the embolic material, the BMF traversed all vascular branches unimpeded, confirming the patency and flow dynamics of the model (Fig. S12a). Nonetheless, complete occlusion was achieved after injecting the APIO/Fe complex hydrogel (Fig. 6d and Fig. S12b). The APIO/Fe complex hydrogel remained localized at injection sites without distal migration, indicating appropriate viscosity and gelation kinetics to achieve controlled embolization. The complete vascular occlusion demonstrated that the APIO/Fe complex hydrogel possesses adequate viscosity for catheter delivery, rapid gelation upon injection, and sufficient mechanical strength to maintain vascular occlusion under physiological pressure gradients, which are essential mechanical properties for effective TACE. Although the BMF used in the 3D vascular model reproduces the viscosity and flow characteristics of blood, it does not fully reflect the biochemical complexity of blood including plasma proteins, competitive chelators or iron ion transport dynamics.[107,108] Therefore, further studies will extend these findings by evaluation under physiologically relevant biochemical conditions *in vivo*.

3. Conclusions

The HA hydrogel incorporating APIO/Fe complexes is a multifunctional embolic agent through the synergistic integration of occlusion, ROS-mediated anticancer therapy and dual CT/MRI capabilities, and complementary therapeutic and diagnostic modalities, thus paving the way for more effective, safer, and personalized minimally invasive cancer treatments that improve patient outcomes and also reduce healthcare costs and procedural complexity.

Physicochemical characterization confirmed stable coordination between APIO CDs and iron ions, forming positively charged nanocomplexes that interact strongly with HA to produce hydrogels with injectability, shear-thinning, and self-healing properties. The hydrogel demonstrated excellent procoagulant activity, promoted rapid thrombus formation, and achieved complete vascular occlusion in 3D dynamic models. It also maintained robust contrast enhancement for real-time procedural guidance and post-treatment monitoring.

This platform addresses critical limitations of current TACE therapies by enabling improved distal vascular penetration, real-time image-guided delivery, and targeted oxidative tumor destruction within a single injectable system. As such, the APIO/Fe hydrogel represents a promising next-generation embolic material poised to improve therapeutic efficacy and clinical outcomes in patients with HCC and beyond.

Author contributions

M. Jin contributed to writing the original draft, investigation, formal analysis and conceptualization. S. Lee contributed to reviewing and editing the original draft, analysis and validation. Y. Na contributed to modelling the 3D vascular model and validation. H. Jung contributed to CT measurements and data validation. D. Kim contributed to conceptualization and experimental validation. K. Na contributed to the supervision, review and editing of the original draft, funding acquisition, and project administration. All authors read and approved the final manuscript.

Conflicts of interest

There are no conflicts to declare.

Data availability

The data supporting the findings of this study are available within the article and its supplementary information (SI). Supplementary information is available. See DOI: https://doi.org/10.1039/d5mh01916h.

Additional raw data, including original imaging files and instrumental characterization data are available from the corresponding author upon reasonable request. No software code was developed or used in this study. All experimental data generated and analyzed during this research comply with the Royal Society of Chemistry data availability policy.

Acknowledgements

This work was supported by the Basic Science Research Program (RS-2022-NR068971) of the National Research Foundation of Korea funded by the Ministry of Science and ICT (MSIT); and the Bio & Medical Technology Development Program of the National Research Foundation (NRF) funded by the Ministry of Science & ICT(RS-2024-00440714).

Notes and references

1 S. Chen, Y. Song, X. Yan, L. Dong, Y. Xu, S. Xuan, Q. Shu, B. Cao, J. Hu and H. Xing, *J. Nanobiotechnol.*, 2022, **20**, 381.
2 W. Wang and C. Wei, *Genes Dis.*, 2020, **7**, 308–319.
3 K. Sankar, J. Gong, A. Osipov, S. A. Miles, K. Kosari, N. N. Nissen, A. E. Hendifar, E. K. Koltsova and J. D. Yang, *Clin. Mol. Hepatol.*, 2023, **30**, 1.

4 S. Brozzetti, C. D'Alterio, S. Bini, J. Antimi, B. Rocco, A. Fassari, P. Lucatelli, P. Nardis, M. Di Martino and G. M. De Sanctis, *Cancers*, 2022, **14**, 4422.
5 I. Angeli-Pahim, A. Chambers, S. Duarte and A. Zarrinpar, *Cancers*, 2023, **15**, 5378.
6 H. Nishikawa, T. Kimura, R. Kita and Y. Osaki, *Int. J. Hyperthermia*, 2013, **29**, 558–568.
7 W. Y. Lau and E. C. Lai, *Ann. Surg.*, 2009, **249**, 20–25.
8 J.-L. Raoul, A. Forner, L. Bolondi, T. T. Cheung, R. Kloeckner and T. de Baere, *Cancer Treat. Rev.*, 2019, **72**, 28–36.
9 A. Massmann, T. Rodt, S. Marquardt, R. Seidel, K. Thomas, F. Wacker, G. M. Richter, H. U. Kauczor, A. Bücker and P. L. Pereira, *Langenbecks Arch. Chir.*, 2015, **400**, 641–659.
10 J. Wu, Z. Zhou, Y. Huang, X. Deng, S. Zheng, S. He, G. Huang, B. Hu, M. Shi and W. Liao, *MedComm*, 2024, **5**, e746.
11 C. Lanza, V. Ascenti, G. V. Amato, G. Pellegrino, S. Triggiani, J. Tintori, C. Intrieri, S. A. Angileri, P. Biondetti and S. Carriero, *J. Clin. Med.*, 2025, **14**, 314.
12 Y. Cho, J. W. Choi, H. Kwon, K. Y. Kim, B. C. Lee, H. H. Chu, D. H. Lee, H. A. Lee, G. M. Kim and J. S. Oh, *J. Liver Cancer*, 2023, **23**, 241–261.
13 J. Hu, H. Albadawi, B. W. Chong, A. R. Deipolyi, R. A. Sheth, A. Khademhosseini and R. Oklu, *Adv. Mater.*, 2019, **31**, 1901071.
14 S. Young, A. S. Larson, P. Torkian and J. Golzarian, *Arab J. Int. Radiol.*, 2022, **6**, 010–014.
15 S. Lee, A. Ghosh, N. Xiao, A. C. Gordon, N. Heidarpour, B. Funaki and R. J. Lewandowski, *Semin. Intervent. Radiol.*, 2023, **40**, 315–322.
16 T. Kojima, T. Maeda, Y. Ito, H. Kikuta and M. Fujii, *J. Neuroendovas. Ther.*, 2025, **19**, 0073.
17 J. Hu, I. Altun, Z. Zhang, H. Albadawi, M. A. Salomao, J. L. Mayer, L. M. P. Hemachandra, S. Rehman and R. Oklu, *Adv. Mater.*, 2020, **32**, 2002611.
18 R. Xie, Y.-C. Chen, Y. Zhao, N. Yodsanit, Y. Wang, N. Yamamoto, D. Yamanouchi and S. Gong, *ACS Appl. Mater. Interfaces*, 2021, **13**, 56988–56999.
19 B. Liu and K. Chen, *Gels*, 2024, **10**, 262.
20 K. Zoeller, D. To and A. Bernkop-Schnuerch, *Biomaterials*, 2025, **312**, 122718.
21 K. Lei, J. Fang, G. Wang and X. Pang, *Sens. Diagn.*, 2025.
22 A. Joshi, S. Choudhury, A. Majhi, S. Parasuram, V. S. Baghel, S. Chauhan, S. Khanra, D. Lahiri and K. Chatterjee, *Biomater. Sci.*, 2025, **13**, 4706–4716.
23 K. Huynh, *Nat. Rev. Cardiol.*, 2017, **14**, 67.
24 D. Jin, Q. Wang, K. F. Chan, N. Xia, H. Yang, Q. Wang, S. C. H. Yu and L. Zhang, *Sci. Adv.*, 2023, **9**, eadf9278.
25 F. Zehtabi, A. Gangrade, K. Tseng, R. Haghniaz, R. Abbasgholizadeh, H. Montazerian, D. Khorsandi, J. Bahari, A. Ahari and N. Mohaghegh, *Adv. Funct. Mater.*, 2023, **33**, 2305880.
26 S. Uman, L. L. Wang, S. L. Thorn, Z. Liu, J. S. Duncan, A. J. Sinusas and J. A. Burdick, *Adv. Healthcare Mater.*, 2020, **9**, 2000294.
27 W. Chang, L. Chen and K. Chen, *Int. J. Biol. Macromol.*, 2024, **270**, 132454.
28 A. R. C. Salih, H. M. U. Farooqi, H. Amin, P. R. Karn, N. Meghani and S. Nagendran, *Future J. Pharm. Sci.*, 2024, **10**, 63.
29 A. B. Hejran, H. Ashrafi, A. Q. Baseer, A. Sarwari, A. W. Monib, M. H. Hassand, S. Sediqi, U. M. Kakar, P. Niazi and M. Rahime, *Eur. J. Theor. Appl. Sci.*, 2024, **2**, 730–743.
30 J. A. Burdick and G. D. Prestwich, *Adv. Mater.*, 2011, **23**, H41–H56.
31 M. Dovedytis, Z. J. Liu and S. Bartlett, *Eng. Regen.*, 2020, **1**, 102–113.
32 X. Xu, A. K. Jha, D. A. Harrington, M. C. Farach-Carson and X. Jia, *Soft Matter*, 2012, **8**, 3280–3294.
33 L.-J. Kang, J. Yoon, J. G. Rho, H. S. Han, S. Lee, Y. S. Oh, H. Kim, E. Kim, S. J. Kim and Y. T. Lim, *Biomaterials*, 2021, **275**, 120967.
34 Y.-W. Ding, Z.-Y. Wang, Z.-W. Ren, X.-W. Zhang and D.-X. Wei, *Biomater. Sci.*, 2022, **10**, 3393–3409.
35 S. Gao, J. Wang, R. Tian, G. Wang, L. Zhang, Y. Li, L. Li, Q. Ma and L. Zhu, *ACS Appl. Mater. Interfaces*, 2017, **9**, 32509–32519.
36 A. Fallacara, E. Baldini, S. Manfredini and S. Vertuani, *Polymers*, 2018, **10**, 701.
37 S. An, S. Choi, S. Min and S.-W. Cho, *Biotechnol. Bioprocess Eng.*, 2021, **26**, 503–516.
38 D. W. Nelson and R. J. Gilbert, *Adv. Healthcare Mater.*, 2021, **10**, 2101329.
39 J. Liu, R. Li and B. Yang, *ACS Cent. Sci.*, 2020, **6**, 2179–2195.
40 Y. Jeong, M. Jin, K. S. Kim and K. Na, *Biomater. Res.*, 2022, **26**, 27.
41 L. Đorđević, F. Arcudi, M. Cacioppo and M. Prato, *Nat. Nanotechnol.*, 2022, **17**, 112–130.
42 N. K. Khairol Anuar, H. L. Tan, Y. P. Lim, M. S. So'aib and N. F. Abu Bakar, *Front. Energy Res.*, 2021, **9**, 626549.
43 H. Su, Y. Liao, F. Wu, X. Sun, H. Liu, K. Wang and X. Zhu, *Colloids Surf., B*, 2018, **170**, 194–200.
44 T. Zhang, Z. Pan, J. Wang, X. Qian, H. Yamashita, Z. Bian and Y. Zhao, *JACS Au*, 2023, **3**, 516–525.
45 H. Li, Y. Dou, H. Yang, H. Xing, C. Zhu, T. Wang, Z. Xuan and M. Yang, *J. Nanobiotechnol.*, 2024, **22**, 100.
46 Y. Zhang, Y. Sun, X. Yang, J. Hilborn, A. Heerschap and D. A. Ossipov, *Macromol. Biosci.*, 2014, **14**, 1249–1259.
47 S. H. Bossmann, M. M. Payne, M. Kalita, R. M. Bristow, A. Afshar and A. S. Perera, *Pharmaceutics*, 2022, **14**, 2093.
48 B. Yu, B. Choi, W. Li and D.-H. Kim, *Nat. Commun.*, 2020, **11**, 3637.
49 L. Wang, H. Guo, W. Zhang, X. Li, Z. Su and X. Huang, *Mater. Today Bio*, 2024, **29**, 101297.
50 J. Seo, J. Lee, C. B. Lee, S. K. Bae and K. Na, *Bioconjugate Chem.*, 2019, **30**, 621–632.
51 X. Wu, L. Wu, X. Cao, Y. Li, A. Liu and S. Liu, *RSC Adv.*, 2018, **8**, 20000–20006.
52 X. Wang, Y. Zhao, T. Wang, Y. Liang, X. Zhao, K. Tang, Y. Guan and H. Wang, *Polymers*, 2021, **13**, 4317.
53 M. Jin, S. Lee, S. B. Lim, M. Lee, J. Park, H. D. Jung, M. H. Kang and K. Na, *Small*, 2025, 2410765.

54 Y. Jeong, H. Shin and K. Na, *ACS Biomater. Sci. Eng.*, 2020, **6**, 6961–6970.
55 A. Grosvenor, B. Kobe, M. C. Biesinger and N. McIntyre, *Surf. Interface Anal.*, 2004, **36**, 1564–1574.
56 T. Yamashita and P. Hayes, *Appl. Surf. Sci.*, 2008, **254**, 2441–2449.
57 C. Brewer, G. Brewer, R. J. Butcher, E. E. Carpenter, L. Cuenca, A. M. Schmiedekamp and C. Viragh, *Dalton Trans.*, 2005, 3617–3619.
58 M. Pascaly, M. Duda, A. Rompel, B. H. Sift, W. Meyer-Klaucke and B. Krebs, *Inorg. Chim. Acta*, 1999, **291**, 289–299.
59 H. H. Jing, F. Bardakci, S. Akgöl, K. Kusat, M. Adnan, M. J. Alam, R. Gupta, S. Sahreen, Y. Chen and S. C. Gopinath, *J. Funct. Biomater.*, 2023, **14**, 27.
60 W. Fawaz, J. Hasian and I. Alghoraibi, *Sci. Rep.*, 2023, **13**, 18641.
61 M. Zhang, H. Ju, L. Zhang, M. Sun, Z. Zhou, Z. Dai, L. Zhang, A. Gong, C. Wu and F. Du, *Int. J. Nanomed.*, 2015, 6943–6953.
62 Z. M. Marković, M. D. Budimir, M. Danko, D. D. Milivojević, P. Kubat, D. Z. Zmejkoski, V. B. Pavlović, M. M. Mojsin, M. J. Stevanović and B. M. T. Marković, *Beilstein J. Nanotechnol.*, 2023, **14**, 165–174.
63 S. Pasieczna-Patkowska, M. Cichy and J. Flieger, *Molecules*, 2025, **30**, 684.
64 J. Coates, *Encycl. Anal. Chem.*, 2000, **12**, 10815–10837.
65 J. D. Stachowska, M. B. Gamża, C. Mellor, E. N. Gibbons, M. J. Krysmann, A. Kelarakis, E. Gumieniczek-Chłopek, T. Strączek, C. Kapusta and A. Szwajca, *Nanomaterials*, 2022, **12**, 674.
66 A. Thirumalai, P. Sharmiladevi, K. Girigoswami, A. D. Prabhu and A. Girigoswami, *ADMET DMPK*, 2025, **13**(5), 2905.
67 N. Santos, P. A. Santana, I. Osorio-Roman, C. Jara-Gutiérrez, J. Villena and M. Ahumada, *RSC Adv.*, 2025, **15**, 12814–12824.
68 A. Kolanowska, G. Dzido, M. Krzywiecki, M. M. Tomczyk, D. Łukowiec, S. Ruczka and S. Boncel, *ACS Omega*, 2022, **7**, 41165–41176.
69 K. Jian, W. Men, C. Miao, Y. Du, H. Yang and X. Zhao, *Talanta*, 2025, **292**, 127942.
70 Z. Yang, Y. Yin, M. Liang, W. Fu, J. Zhang, F. Liu, W. Zhang and B. Pan, *Nat. Commun.*, 2025, **16**, 146.
71 P. García-Negueroles, S. García-Ballesteros, A. M. Amat, E. Laurenti, A. Arques and L. Santos-Juanes, *ACS Omega*, 2019, **4**, 21698–21703.
72 Y. Nie, Y. Zhang, X. Nie, X. Tian, C. Dai and J. Shi, *J. Hazard. Mater.*, 2023, **448**, 130949.
73 M. Wang, Y. Ruan, X. Xing, Q. Chen, Y. Peng and J. Cai, *Anal. Chim. Acta*, 2011, **697**, 83–89.
74 M. Hanke-Roos, K. Fuchs, S. Maleschlijski, J. Sleeman, V. Orian-Rousseau and A. Rosenhahn, *Cell Adhes. Migr.*, 2017, **11**, 476–487.
75 M. Yusupov, A. Privat-Maldonado, R. M. Cordeiro, H. Verswyvel, P. Shaw, J. Razzokov, E. Smits and A. Bogaerts, *Redox Biol.*, 2021, **43**, 101968.
76 T. Ando, J. Yamasaki, H. Saya and O. Nagano, *Stem Cells*, 2025, **43**, sxaf024.
77 D. Tang, X. Chen, R. Kang and G. Kroemer, *Cell Res.*, 2021, **31**, 107–125.
78 S. Franco, L. Severini, E. Buratti, L. Tavagnacco, S. Sennato, L. Micheli, M. Missori, B. Ruzicka, C. Mazzuca and E. Zaccarelli, *Carbohydr. Polym.*, 2025, **354**, 123329.
79 S. M. Hashemnejad and S. Kundu, *Soft Matter*, 2019, **15**, 7852–7862.
80 X.-E. Hu, Y.-R. Shi, X. Zhu, K.-W. Tian and X.-L. Xu, *J. Drug Delivery Sci. Technol.*, 2023, **80**, 104107.
81 S. Hou and P. X. Ma, *Chem. Mater.*, 2015, **27**, 7627–7635.
82 A. Lenoch, M. Schönhoff and C. Cramer, *Soft Matter*, 2022, **18**, 8467–8475.
83 S. Zhu, Y. Wang, Z. Wang, L. Chen, F. Zhu, Y. Ye, Y. Zheng, W. Yu and Q. Zheng, *Gels*, 2023, **9**, 145.
84 Z. Li, J. Lu, T. Ji, Y. Xue, L. Zhao, K. Zhao, B. Jia, B. Wang, J. Wang and S. Zhang, *Adv. Mater.*, 2024, **36**, 2306350.
85 P. Bertsch, M. Diba, D. J. Mooney and S. C. Leeuwenburgh, *Chem. Rev.*, 2022, **123**, 834–873.
86 C. Wang, D. Zhao, Y. Xie, Q. Zhou and H. Yang, *RSC Adv.*, 2023, **13**, 35985–35991.
87 P. Snetkov, K. Zakharova, S. Morozkina, R. Olekhnovich and M. Uspenskaya, *Polymers*, 2020, **12**, 1800.
88 T. Yazdanparast, A. Ayatollahi, A. Samadi, A. Sabzvari, H. Kafi and A. Firooz, *J. Cosmet. Dermatol.*, 2025, **24**, e70117.
89 Y. Han, D. Li, D. Li, W. Chen, S. E. Mu, Y. Chen and J. Chai, *Sci. Rep.*, 2020, **10**, 1858.
90 F. Shuai, Y. Zhang, Y. Yin, H. Zhao and X. Han, *Carbohydr. Polym.*, 2021, **260**, 117777.
91 J. Ryu, S. Kim, I. Oh, S. Kato, T. Kosuge, A. V. Sokolova, J. Lee, H. Otsuka and D. Sohn, *Macromolecules*, 2019, **52**, 6502–6513.
92 G. A. Parada and X. Zhao, *Soft Matter*, 2018, **14**, 5186–5196.
93 R. Prasad, P. S. Marotrao, V. S. Sheorain and S. Gamanagatti, *J. Clin. Interv. Radiol. ISVIR*, 2024, **8**, 149–155.
94 Y. Jiang, Y. Zhang, Z. Lu, X. Wang, S. Bai, Y. Chen, J. Mao and G. Liu, *ChemPhysMater*, 2022, **1**, 39–50.
95 A. Pal, J. Blanzy, K. J. R. Gómez, M. C. Preul and B. L. Vernon, *Gels*, 2023, **9**, 378.
96 T. E. Robinson, E. A. B. Hughes, A. Bose, E. A. Cornish, J. Y. Teo, N. M. Eisenstein, L. M. Grover and S. C. Cox, *Adv. Healthcare Mater.*, 2020, **9**, 1901521.
97 M. H. Chen, L. L. Wang, J. J. Chung, Y.-H. Kim, P. Atluri and J. A. Burdick, *ACS Biomater. Sci. Eng.*, 2017, **3**, 3146–3160.
98 A. Béduer, F. Bonini, C. A. Verheyen, M. Genta, M. Martins, J. Brefie-Guth, J. Tratwal, A. Filippova, P. Burch and O. Naveiras, *Adv. Mater.*, 2021, **33**, 2102350.
99 X. Zhu, M. Duan, L. Zhang, J. Zhao, S. Yang, R. Shen, S. Chen, L. Fan and J. Liu, *Adv. Funct. Mater.*, 2023, **33**, 2209413.
100 S. Wu, K. Fan, Q. Yang, Z. Chen, Y. Hou, Y. Zou, W. Cai and L. Kang, *J. Nanobiotechnol.*, 2023, **21**, 42.
101 A. Hagit, B. Soenke, B. Johannes and M. Shlomo, *Biomacromolecules*, 2010, **11**, 1600–1607.
102 R. Haghniaz, H. Montazerian, A. Rabbani, A. Baidya, B. Usui, Y. Zhu, M. Tavafoghi, F. Wahid, H. J. Kim and A. Sheikhi, *Adv. Healthcare Mater.*, 2023, **12**, 2301551.

103 L. Cui, J. Li, S. Guan, K. Zhang, K. Zhang and J. Li, *Mater. Today Bio*, 2022, **14**, 100257.
104 W. Yang, X. Kang, X. Gao, Y. Zhuang, C. Fan, H. Shen, Y. Chen and J. Dai, *Adv. Funct. Mater.*, 2023, **33**, 2211340.
105 X. Xia, X. Xu, B. Wang, D. Zhou, W. Zhang, X. Xie, H. Lai, J. Xue, A. Rai and Z. Li, *Adv. Funct. Mater.*, 2022, **32**, 2109332.
106 M. Suneetha, K. M. Rao and S. S. Han, *ACS Omega*, 2019, **4**, 12647–12656.
107 K. K. Dakok, M. Z. Matjafri, N. Suardi, A. A. Oglat and S. E. Nabasu, *J. Ultrasonography*, 2021, **21**, e219.
108 A. A. Oglat, M. Matjafri, N. Suardi, M. A. Abdelrahman, M. A. Oqlat and A. A. Oqlat, *J. Med. Ultrasound*, 2018, **26**, 134–142.